SCIENCE CHINA
Earth Sciences

•RESEARCH PAPER•

August 2021 Vol.64 No.8: 1305–1317
https://doi.org/10.1007/s11430-020-9744-6

In situ cosmogenic ^{10}Be, ^{26}Al, and ^{21}Ne dating in sediments from the Guizhou Plateau, southwest China

Ye YANG[1,2], Yu LIU[3], Yan MA[4], Sheng XU[1,2*], Cong-Qiang LIU[1†], Shi-Jie WANG[3],
Finlay M. STUART[2] & Derek FABEL[2]

[1] *Institute of Surface-Earth System Science, School of Earth System Science, Tianjin University, Tianjin 300072, China;*
[2] *Scottish Universities Environmental Research Centre, East Kilbride G75 0QF, UK;*
[3] *State Key Laboratory of Environmental Geochemistry, Institute of Geochemistry, Chinese Academy of Sciences, Guiyang 550081, China;*
[4] *State Key Laboratory of Earthquake Dynamics, Institute of Geology, China Earthquake Administration, Beijing 100029, China*

Received August 14, 2020; revised January 5, 2021; accepted February 11, 2021; published online June 30, 2021

Abstract Landscape evolution is modulated by the regional tectonic uplift, climate change, and river dynamics. However, how to distinguish these mechanisms through the research of surface exhumation and fluvial incision remains controversial. In this study, cosmogenic ^{10}Be, ^{26}Al, and ^{21}Ne concentrations in quartz from cave deposits, modern river sediments, and bedrocks were measured to constrain the applicability of cosmogenic ^{21}Ne and discuss Quaternary landscape evolution history in the Guizhou Plateau, southeast China. Using the ^{26}Al-^{10}Be and ^{21}Ne-^{10}Be pairs to distinguish the cosmogenic ^{21}Ne concentration from the excess ^{21}Ne, we found that the nucleogenic ^{21}Ne produced by the U and Th decay in quartz is significant in the samples although there is the possibility of inherited cosmogenic ^{21}Ne. Combining with previous studies, we suggest that the precise approach for applying the cosmogenic ^{21}Ne could be reached by (1) estimating the contribution from nucleogenic ^{21}Ne, (2) avoiding samples with complex burial histories to exclude inherited cosmogenic ^{21}Ne, and (3) combining the ^{10}Be-^{26}Al-^{21}Ne nuclides method for the Quaternary samples. In addition, both pre-burial basin denudation rates and burial ages derived from the ^{26}Al-^{10}Be pair were used to determine the different timescale surface denudation rate and fluvial incision rate in relation to previous work. The consistency of the different timescales pre-burial basin denudation rate, ^{36}Cl surface denudation rate, and modern basin denudation rate indicates that the landscape-scale surface denudation has been likely stabilized since the Quaternary in the Guizhou Plateau area. The slightly higher river incision rates than the local surface denudation rate show that the river dynamics may not have reached a steady-state due to the regional tectonic uplift in the Guizhou Plateau.

Keywords Cosmogenic ^{10}Be-^{26}Al-^{21}Ne, Burial dating, Incision rate, Landscape evolution, Guizhou Plateau

Citation: Yang Y, Liu Y, Ma Y, Xu S, Liu C Q, Wang S J, Stuart F M, Fabel D. 2021. *In situ* cosmogenic ^{10}Be, ^{26}Al, and ^{21}Ne dating in sediments from the Guizhou Plateau, southwest China. Science China Earth Sciences, 64(8): 1305–1317, https://doi.org/10.1007/s11430-020-9744-6

1. Introduction

Terrestrial *in situ* cosmogenic nuclides (TCN) are widely applied in surface Earth sciences, such as exposure dating, denudation rate calculation, and burial dating (e.g. Dunai, 2010). Single nuclide measured in the suitable mineral target can be sufficiently used to determine the surface exposure ages or basin-wide denudation rates (e.g. Gosse and Phillips, 2001). The analysis of paired nuclides with different half-lives allows the estimation of burial ages and pre-burial basin denudation rates when sediments are buried deeply and rapidly enough to prevent TCN production after burial (Lal, 1991; Granger and Muzikar, 2001). The ^{26}Al-^{10}Be pair is widely used in dating Pleistocene sediments. Coupling cosmogenic ^{21}Ne, produced in quartz, with ^{26}Al or ^{10}Be could

---

* Corresponding author (email: sheng.xu@tju.edu.cn)
† Corresponding author (email: liucongqiang@tju.edu.cn)

improve the age range and accuracy of ^{26}Al-^{10}Be burial dating (Balco and Shuster, 2009a). Over the past two decades, studies in the analytical procedures and determination of the different sources of Ne in quartz have been well established (Niedermann, 2002; Codilean et al., 2008; Balco and Shuster, 2009b; Heber et al., 2009; Vermeesch et al., 2015). However, only a few works have been done in the sediment burial dating by using the ^{21}Ne-^{26}Al and ^{21}Ne-^{10}Be pairs (Balco and Shuster, 2009a; Davis et al., 2011; Matmon et al., 2014; McPhillips et al., 2016; Ma et al., 2018; Sartégou et al., 2018; Ben-Israel et al., 2020). It is due to the difficulty to measure the cosmogenic ^{21}Ne from a complex three-component mixing of atmospheric, cosmogenic, and nucleogenic neon. Recently, some previous studies also realized that the production due to the capture of alpha particles derived from the decay of naturally occurring U and Th in minerals via the reaction ^{18}O(α, n) ^{21}Ne is non-negligible (Ben-Israel et al., 2018; Balco et al., 2019; Balter-Kennedy et al., 2020), henceforth called "nucleogenic ^{21}Ne", which is regarded as the main obstruction for accurate measurement of the amount of cosmogenic ^{21}Ne. This paper describes TCN measurements of ^{10}Be, ^{26}Al, and ^{21}Ne abundance in quartz in cave deposits, sandstone bedrocks, and modern fluvial sediments collected from karst landforms in the Guizhou Plateau, which is a broad upland region separating the Yangtze River and Pearl River in southwestern China (Figure 1a). The integrated paleo-denudation rates in different timescales and sediment burial ages were presented to determine the surface denudation rate and fluvial incision rate in the Guizhou Plateau, respectively, in relation to the results of water chemistry data (Han and Liu, 2004; Xu and Liu, 2010) and TCN ^{36}Cl (Xu et al., 2013; Yang et al., 2020). The purposes of the paper are: (1) to quantify ^{21}Ne in quartz in relation to cosmogenic ^{21}Ne calculated from the ^{10}Be-^{26}Al pair burial ages and nucleogenic ^{21}Ne from the alpha capture reactions due to decay of U and Th; (2) to discuss the

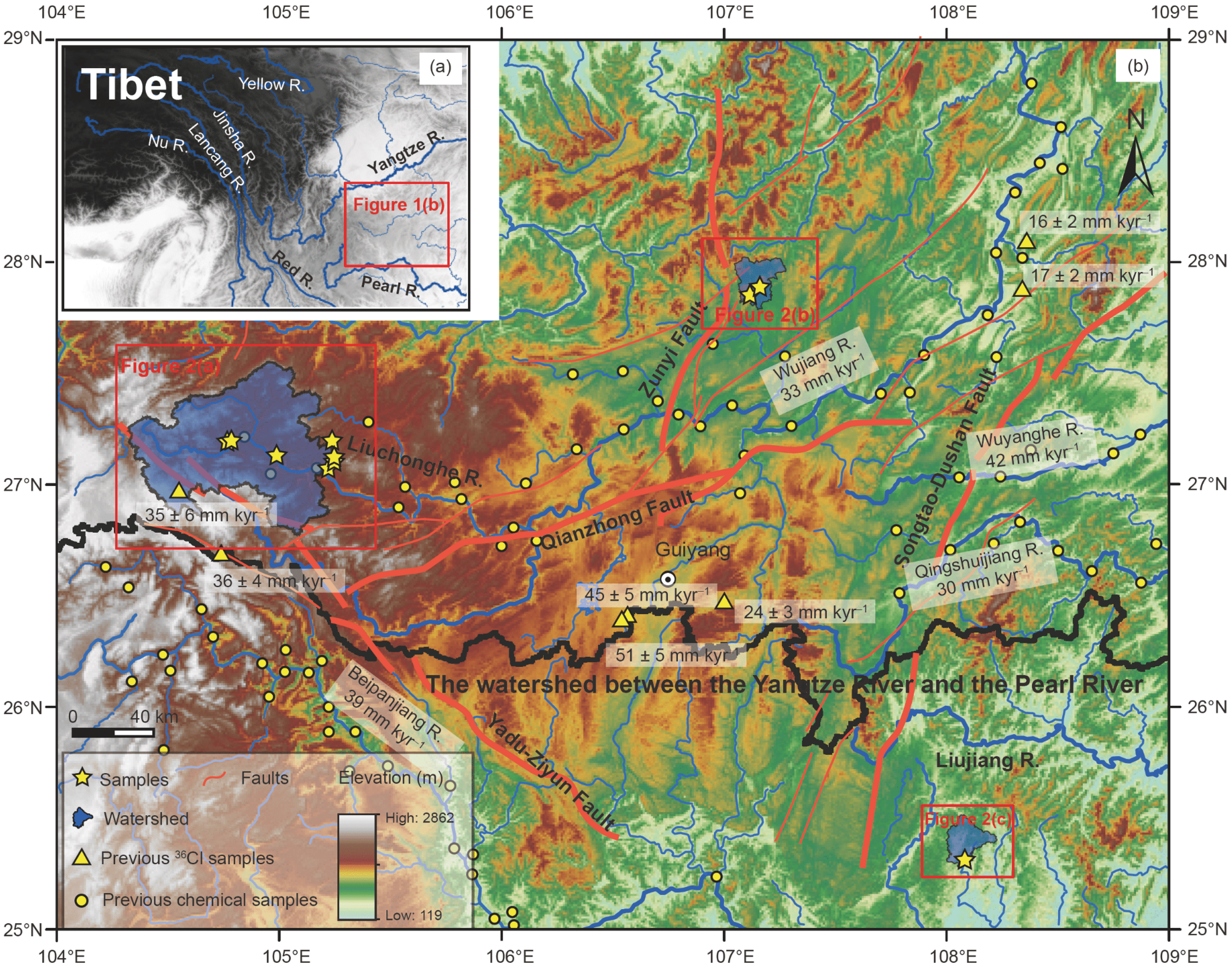

Figure 1 Topographic map of the Guizhou Plateau based on 30-m-resolution Shuttle Radar Topography Mission (SRTM) digital elevation model, showing the major river distributions and previous carbonate denudation rates estimated from TCN ^{36}Cl (Xu et al., 2013; Yang et al., 2020). The denudation rates below the river names are derived from the water chemistry data (Han and Liu, 2004; Xu and Liu, 2010). The black line shows the watershed between the Yangtze River and the Pearl River.

Quaternary landscape evolution and tectonic uplift in the Guizhou Plateau.

2. Geological setting and sampling descriptions

2.1 Study region

The southeastern margin of the Tibetan Plateau is characterized by a low-gradient topographic surface (Clark et al., 2004; Liu-Zeng et al., 2008) that is mainly drained by the Red, Middle Yangtze, and Pearl rivers (Figure 1a). The Guizhou Plateau, located in the most southeastern margin of the Tibetan Plateau (Figure 1b), is regarded as a natural experimental field to study the regional tectonic uplift, surface landform denudation, and fluvial incision, which can be used as a proxy for the timing of initial uplift (Clark et al., 2005). The study region ranges in altitude from ~100 m above sea level (a.s.l.) in the east to nearly 3,000 m a.s.l. in the west, and over 500,000 km^2 of its surface is limestone karst (Figure 1b). The carbonate bedrock formed a stable karst landform from the Late Proterozoic to the end of the Middle Triassic. Study sites lie on the drainage divide between the Wujiang River (a tributary of the Yangtze River) and the Beipanjiang River (a tributary of the Pearl River) (Figure 1b). These rivers and their major tributaries have cut deep into the plateau to form valleys and canyons with steep sides (Smart et al., 1985), where an abundance of multilevel caves are well developed. For discussing the spatial and temporal variation of the caves, fifteen samples including cave deposits, modern river sediments, and bedrocks were collected along an elevation gradient (from ~1700 to ~600 m a.s.l.) in the Guizhou Plateau (Table 1), of which nine ^{10}Be and ^{26}Al results have been published elsewhere (Table 2; Liu et al., 2013a, 2013b).

2.2 Sampling strategy

Eight samples including five cave deposits and three modern river sediments were collected by Liu et al. (2013b) along the Liuchonghe River (a northern tributary of the Wujiang River) (Figure 2a). We did a further field campaign for sampling sandstone bedrocks (HZ1, HZ2, and TB1) to calibrate the nucleogenic ^{21}Ne. Sandstone bedrocks, covered by 10 m-thick Jurassic strata, were collected from the artificial road cut profiles (Figure 3a–3c). The cave deposits of MWC (1130±5 m a.s.l.) and MDC (925±5 m a.s.l.) are 90±5 m and 34±5 m higher than the nearest river erosion datum, respectively (Figure 2b and Figure 3d–3e). The HC sampling site was well described in Liu et al. (2013a), in which the cave deposit (608±5 m a.s.l.) is 43±5 m higher than the nearest Sanchahe River erosion datum (Figure 2c). All modern sediments and cave deposits are composed of pebbles, sand, and silt. The sandstone pebbles with similar sizes were selected to avoid the complex mixing of quartz from different source areas. All deeply buried cave deposits (>20 m) were collected from main open-channel deposits in lateral erosion and water table caves, except for the sample of DYC from a branching cave.

3. Analytical methods

3.1 Sample preparation and analyses

All the samples were crushed and sieved to fractions of 250–500 μm, followed by magnetic separations. Oxides and carbonate matter were removed by HCl/HNO$_3$ leaching. Multiple overnight leaches in hot 2% HF/HNO$_3$ solutions were performed to remove the meteoric cosmogenic nuclides and to obtain purified quartz that Al concentration is below 150 ppm (1 ppm=1 μg/g). Chemical preparation was performed at the Scottish Universities Environmental Research Centre (SUERC) following a modified version of the protocol of Kohl and Nishiizumi (1992). Details of the chemical procedure can be referred to elsewhere (Liu et al., 2013b). ^{10}Be/^{9}Be and ^{26}Al/^{27}Al ratios were measured at the SUERC accelerator mass spectrometers (AMS) facility, using NIST SRM 4325 with a nominal ^{10}Be/^{9}Be value of 2.79×10^{-11} and Z92-0222 with a nominal ^{26}Al/^{27}Al value of 4.11×10^{-11}, respectively. ^{10}Be/^{9}Be and ^{26}Al/^{27}Al ratios were corrected from a full chemical procedural blank. ^{27}Al has been measured by inductively coupled plasma atomic emission spectrometry (ICP-OES).

Seventeen clean quartz samples, including two duplicate samples (DSC-d and YTGC-d), were treated further for neon isotope measurement. Chemical preparation was carried out at SUERC following standard methods (Codilean et al., 2008; Vermeesch et al., 2015; Ma et al., 2018). About 200 mg of quartz was rinsed in ultra-pure acetone and encapsulated into an aluminum foil cylinder. Due to the relatively low measurement precision of isotope ^{22}Ne, it is hard to discriminate between cosmogenic and non-cosmogenic components based on their isotopic signatures. Although the stepwise heating method was expected to solve this problem (Niedermann, 2002), a quantitative separation of different components is seldom possible because the significant contribution of nucleogenic ^{21}Ne was also found at temperatures <600°C (Schäfer et al., 2002). Hence, the neon was extracted by one-step heating at 1350°C for 25 min in this study. Neon isotopes were analyzed statically in a Mass Analyser Products MAP-215 magnetic sector mass spectrometer at SUERC. Isobaric interference $H^{19}F^{+}$ and $^{40}Ar^{2+}$ on mass 20 and $^{12}C^{16}O_2^{2+}$ on mass 22 were corrected by calculating the measured $^{19}F^{+}$, $^{40}Ar^{+}$, and $^{12}C^{16}O_2^{+}$ signals, respectively. The isobaric interference $H_2^{18}O^{+}$ on mass 20 and $^{65}Cu^{3+}$ on mass 21 can be ignored. The results were calibrated versus the quartz standard CREU-1 (Vermeesch et al., 2015). The

Table 1 Sampling information and the measured ^{10}Be, ^{26}Al, and ^{21}Ne results[a)]

Sample	Longitude (E)	Latitude (N)	Elevation (m)	Sample type	Scaling factor[c)]	Height above river[d)] (m)	^{10}Be and ^{26}Al quartz mass (g)	^{21}Ne quartz mass (mg)	Al (ppm)	Be carrier (mg)	^{10}Be/^{9}Be ($\times10^{-13}$)	^{26}Al/^{27}Al ($\times10^{-13}$)	^{20}Ne ($\times10^{10}$ at g^{-1})	^{22}Ne/^{20}Ne	Error	^{21}Ne/^{20}Ne	Error
River sediments (pebbles, sand, and silt)																	
MDC-RB	107.1254°	27.8891°	891	Sandstone pebbles	1.57	0	17.827	212.1	223.1	0.2216	2.51	2.71	5.19	0.1021	0.0005	0.00313	0.00004
SXC-RB	104.9529°	27.1345°	1221	Sandstone pebbles	3.04	0	22.821	206.7	155.7	0.2162	1.65	1.75	7.03	0.1021	0.0003	0.00302	0.00003
DSC-RB	105.2024°	27.1999°	1512	Sandstone pebbles	3.04	0	23.586	255.7	146.9	0.2189	3.33	4.17	5.81	0.1018	0.0003	0.00302	0.00005
YTGC-RB	105.2095°	27.1098°	1398	Sandstone pebbles	3.04	0	24.446	209.8	127.6	0.2175	1.53	1.78	5.20	0.1023	0.0004	0.00324	0.00004
Cave deposits (pebbles, sand, and silt)																	
MWC	107.0816°	27.8548°	1130	Sandstone pebbles	1.86	90±5	18.700	203.0	199.9	0.2218	6.20	6.00	3.88	0.1026	0.0005	0.00331	0.00004
MDC	107.1254°	27.8891°	925	Sandstone pebbles	1.61	34±5	17.776	209.0	209.5	0.2209	7.11	7.29	4.62	0.1025	0.0006	0.00320	0.00004
SXC	104.9529°	27.1345°	1397	Sandstone pebbles	3.04	199±5	23.823	222.0	242.0	0.2176	0.14	0.05	6.05	0.1021	0.0006	0.00304	0.00002
DYC	105.1846°	27.0736°	1285	Sandstone pebbles	3.04	145±5	20.549	218.0	187.2	0.2188	1.19	0.35	4.64	0.1024	0.0006	0.00312	0.00006
DSC	105.2020°	27.1999°	1562	Sandstone pebbles	3.04	50±5	21.949	241.0	197.6	0.2157	2.91	2.01	4.60	0.1022	0.0002	0.00303	0.00003
DSC-d[b)]							–	195.5	–	–	–	–	5.61	0.1022	0.0005	0.00303	0.00002
DSC-S	105.2020°	27.1999°	1562	Coarse sand	3.04	50±5	21.986	241.1	131.9	0.2177	4.22	4.49	5.73	0.1023	0.0003	0.00312	0.00002
YTGC	105.2095°	27.1098°	1488	Sandstone pebbles	3.04	90±5	19.484	230.1	190.7	0.2176	1.67	1.53	6.38	0.1019	0.0003	0.00311	0.00002
YTGC-d[b)]								206.6	–	–	–	–	6.17	0.1021	0.0004	0.00311	0.00003
HC	108.0470°	25.3142°	608	Sandstone pebbles	1.25	43±5	19.222	198.0	201.0	0.2213	0.51	0.33	6.05	0.1019	0.0006	0.00314	0.00004
Bedrocks (sandstone)																	
HZ1	104.7300°	27.1916°	1486	Sandstone (J_1)	2.36	26±5	19.316	274.8	–	0.2210	0.089	–	2.68	0.1031	0.0007	0.00368	0.00005
HZ2	104.7506°	27.1963°	1693	Sandstone (J_1)	2.72	233±5	–	207.1	–	–	–	–	5.97	0.1021	0.0002	0.00315	0.00002
TB1	105.2074°	27.1238°	1567	Sandstone (J_2)	2.51	117±5	–	179.0	–	–	–	–	6.50	0.1023	0.0002	0.00310	0.00003

a) The Ne is the total Ne measured. The neon was extracted by one-step heating at 1350°C for 25 min. ^{10}Be and ^{26}Al concentrations in samples SXC-RB, DSC-RB, YTGC-RB, SXC, DYC, DSC, DSC-S, and YTGC are from Liu et al. (2013b) and those in HC from Liu et al. (2013a). b) Duplicate measurements are carried out to test the repeatability of the ^{21}Ne experimental procedure. c) The scaling factor derived from Stone (2000) is calculated by the averaged basin elevation. d) The height above river assuming a maximum error of 5 m is measured by a laser range finder.

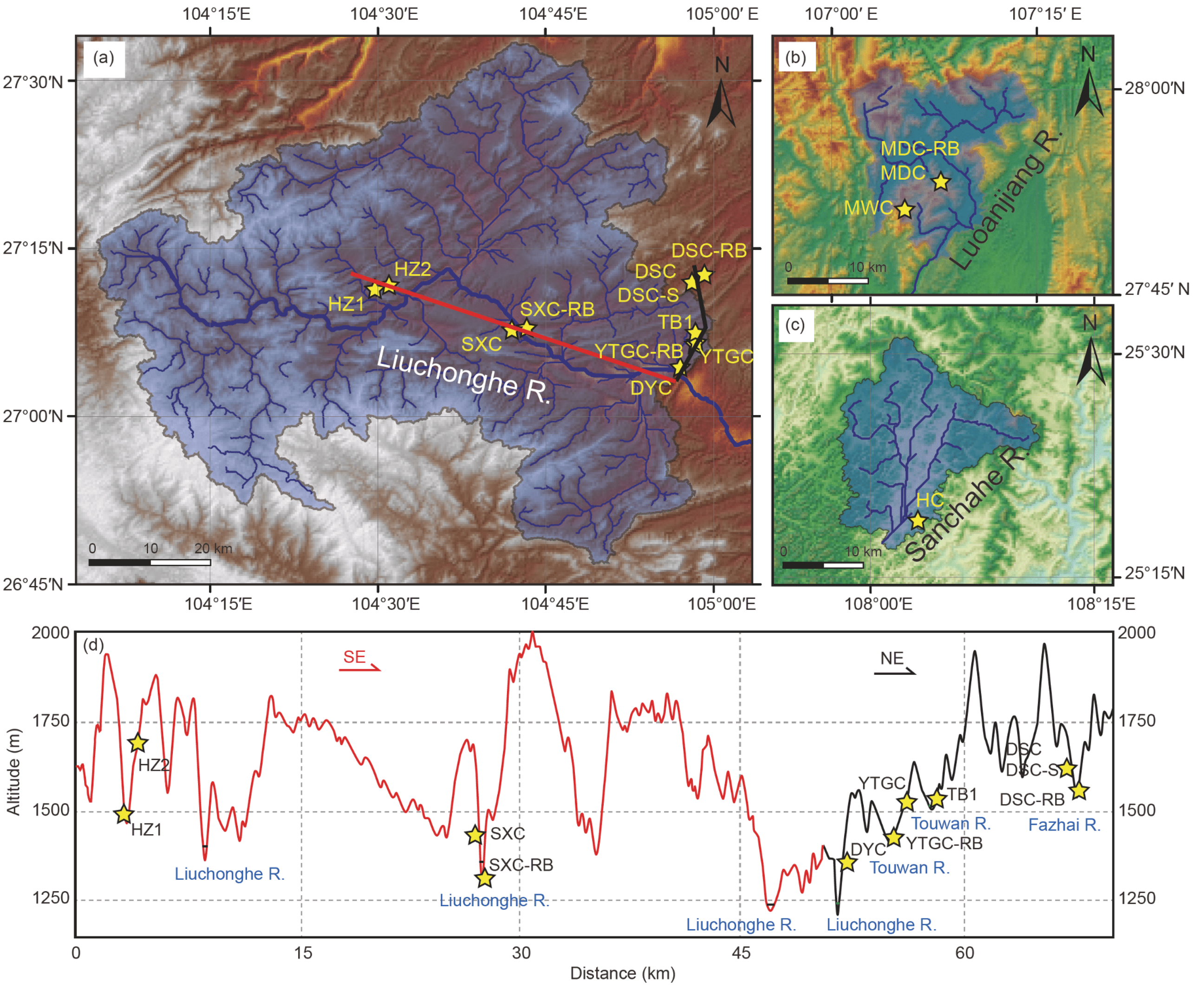

Figure 2 (a)–(c) Sampling locations and watershed areas. (d) Longitudinal profile shows the vertical distribution of sampling sites and the landscape relief. The red and black lines in (a) are the position of longitudinal profile in (d).

abundance of cosmogenic ^{21}Ne was calculated by assuming three-component mixing of atmospheric, cosmogenic, and nucleogenic neon (Niedermann, 2002; Balco et al., 2019), and no neon blank correction has been made to the data. The excess $^{21}\mathrm{Ne}_{\mathrm{ex}}$ including both cosmogenic and nucleogenic neon was calculated by the following equation:

$$^{21}\mathrm{Ne}_{\mathrm{ex}} = {}^{20}\mathrm{Ne}_{\mathrm{m}} \times \left[\left({}^{21}\mathrm{Ne}/{}^{20}\mathrm{Ne}\right)_{\mathrm{m}} - \left({}^{21}\mathrm{Ne}/{}^{20}\mathrm{Ne}\right)_{\mathrm{a}}\right], \qquad (1)$$

where $^{20}\mathrm{Ne}_{\mathrm{m}}$ is the measured value of ^{20}Ne, $(^{21}\mathrm{Ne}/^{20}\mathrm{Ne})_{\mathrm{m}}$ is the measured $^{21}\mathrm{Ne}/^{20}\mathrm{Ne}$ ratio, and $(^{21}\mathrm{Ne}/^{20}\mathrm{Ne})_{\mathrm{a}}$ is the $^{21}\mathrm{Ne}/^{20}\mathrm{Ne}$ ratio in the atmosphere, which we take to be 0.002959 (Eberhardt et al., 1965). This equation is approximately assuming that the excess ^{20}Ne is negligible.

The nucleogenic ^{21}Ne due to U and Th decay is described as (Ben-Israel et al., 2018; Balco et al., 2019):

$$C_{21,\mathrm{nuc}}(t_{\mathrm{c}}) = \sum_i f_i F_{\mathrm{T},i} Y_{\alpha,i} N_i \left(\mathrm{e}^{\lambda_i t_{\mathrm{c}}} - 1\right), \qquad (2)$$

where $C_{21,\mathrm{nuc}}(t_{\mathrm{c}})$ is the nucleogenic ^{21}Ne concentration since the closure age of t_{c}, and i is the radionuclide including ^{238}U, ^{235}U, and ^{232}Th. f_i is the fraction factor of alpha particles produced from decay of nuclide i, where $f_{238} = 4.04\times10^{-8}$, $f_{235} = 5.62\times10^{-8}$, and $f_{232} = 6.08\times10^{-8}$ (Cox et al., 2015). $F_{\mathrm{T},i}$ is the factor to describe the ejected alpha particles at grain boundaries, and $F_{\mathrm{T},i} = 1$ is taken here by assuming that the HF leaching completely removed the alpha-depleted grain boundaries (Balco et al., 2019). $Y_{\alpha,i}$ is the number of alpha particles throughout the decay chain of nuclide i ($Y_{\alpha,238} = 8$, $Y_{\alpha,235} = 7$, and $Y_{\alpha,232} = 6$) with the assumption of secular equilibrium, N_i is the concentration (at g^{-1}) of measured ^{238}U, ^{235}U, and ^{232}Th, and λ_i is the decay constant of i. For accessing the nucleogenic ^{21}Ne concentration, we assume that both cosmogenic ^{21}Ne from the initial exposure of the bedrock sandstone and nucleogenic ^{21}Ne inventory has been lost during the reheating mineralization event in relation to the formation of ~235 Ma Pb-Zn deposits in this area (Hu and Zhou, 2012) (see detailed discussion in Section 5.1).

Table 2 Calculation results of ^{10}Be, ^{26}Al and ^{21}Ne

Sample	[^{10}Be] ($\times10^3$ at g^{-1})	[^{26}Al] ($\times10^4$ at g^{-1})	[^{21}Ne$_{ex}$] ($\times10^6$ at g^{-1})	^{26}Al/^{10}Be	^{10}Be/^{21}Ne ($\times10^{-2}$)	^{10}Be-^{26}Al$^{b)}$ (Ma)	Denudation rate$^{b)}$ (mm kyr^{-1})	^{10}Be-^{21}Ne$^{c)}$ (Ma)	Nucleogenic ^{21}Ne$^{d)}$ ($\times10^6$ at g^{-1})	Incision rate (mm kyr^{-1})
River sediments										
MDC-RB	200.8±6.5	134.1±4.8	8.3±2.3	6.68±0.32	2.41±0.67	$0.00^{+0.08}_{-0.00}$	$18.4^{+1.4}_{-1.3}$	4.40±0.48	7.47 (89.7%)	–
SXC-RB$^{a)}$	101.3±3.5	60.3±2.4	3.7±2.1	5.95±0.31	2.7±1.5	$0.25^{+0.10}_{-0.11}$	$62.6^{+5.2}_{-4.7}$	4.4±1.1	3.24 (86.9%)	–
DSC-RB$^{a)}$	203.9±6.2	136.3±4.9	3.1±1.2	6.68±0.31	6.6±2.6	$0.00^{+0.10}_{-0.00}$	$35.1^{+2.5}_{-2.4}$	2.60±0.75	2.22 (71.8%)	–
YTGC-RB$^{a)}$	88.3±3.4	50.3±2.1	14.4±2.0	5.69±0.32	0.612±0.089	$0.34^{+0.12}_{-0.11}$	$68.6^{+6.5}_{-5.7}$	7.15±0.26	13.97 (96.9%)	–
Cave deposits										
MWC	478±14	266.9±8.3	13.26±0.46	5.58±0.24	3.60±0.17	$0.32^{+0.08}_{-0.09}$	$7.60^{+0.55}_{-0.51}$	3.48±0.08	10.80 (81.4%)	281±81
MDC	576±18	340±11	10.83±0.36	5.91±0.26	5.32±0.25	$0.18^{+0.08}_{-0.09}$	$5.78^{+0.45}_{-0.39}$	2.72± 0.08	8.03 (74.1%)	189±98
SXC$^{a)}$	6.1±1.3	2.0±0.9	4.86±0.15	3.4±1.6	0.125±0.026	$1.45^{+1.13}_{-0.87}$	580^{+450}_{-280}	10.53±0.42	4.81 (98.9%)	137±82
DYC$^{a)}$	81.4±3.2	13.7±1.3	7.24±0.28	1.68±0.17	1.142±0.062	$2.84^{+0.21}_{-0.20}$	$21.3^{+2.7}_{-2.5}$	6.07±0.11	5.80 (80.2%)	51.1±4.0
DSC$^{a)}$	188.4±6.1	87.9±3.2	3.3±1.5	4.68±0.23	6.2±2.5	$0.74^{+0.10}_{-0.10}$	$26.2^{+2.1}_{-1.9}$	2.86±0.45	1.86 (61.5%)	68±11
DSC-S$^{a)}$	276.0±8.9	131.8±4.7	8.7±1.0	4.77±0.23	3.17±0.40	$0.68^{+0.10}_{-0.09}$	$18.3^{+1.5}_{-1.3}$	3.96±0.23	7.03 (80.8%)	74±12
YTGC$^{a)}$	121.3±4.6	64.5±3.2	9.1±2.3	5.31±0.33	1.27 ±0.21	$0.48^{+0.13}_{-0.13}$	$46.5^{+4.6}_{-4.0}$	5.70±0.24	9.91 (93.1%)	186±52
HC$^{a)}$	33.5±2.3	13.8±1.3	10.54±0.36	4.13±0.47	0.318±0.024	$1.01^{+0.23}_{-0.23}$	$53.4^{+9.5}_{-8.3}$	8.28±0.15	10.30 (97.8%)	43 ±11
Bedrocks										
HZ1	6.8±1.8	–	19.1±1.4	–	0.036±0.010	–	–	12.68±0.53	–	–
HZ2	–	–	11.3±1.2	–	–	–	–	–	–	–
TB1	–	–	9.4±2.9	–	–	–	–	–	–	–

a) ^{10}Be and ^{26}Al concentrations in samples SXC-RB, DSC-RB, YTGC-RB, SXC, DYC, DSC, DSC-S; and TYGC are from Liu et al. (2013b) and those in HC from Liu et al. (2013a). b) ^{10}Be-^{26}Al burial ages and pre-burial basin denudation rates are calculated according to eqs. (5a) and (5b) using the Monte Carlo simulation (see detail in Section 3.2). c) ^{10}Be-^{21}Ne burial ages are derived from a total ^{21}Ne$_{ex}$ (cosmogenic and nucleogenic Ne). d) Nucleogenic ^{21}Ne is estimated according to the equation of ^{21}Ne$_{nucleogenic}$ = ^{21}Ne$_{excess}$$-P/(\rho\varepsilon/\Lambda)$, where ε is pre-burial basin denudation rate derived from the ^{26}Al-^{10}Be pair, P is the pre-burial basin ^{21}Ne production rate.

3.2 Paired-cosmogenic nuclides burial dating

The expression of a measured nuclide concentration at or near the Earth's surface as a function of denudation rate (ε) and exposure age (t) can be described by the following equation (Lal, 1991; Yang et al., 2019):

$$C(x,\varepsilon,t) = C(x,0)\mathrm{e}^{-\lambda t} + \sum_{i=\mathrm{spal,slow,fast}} \frac{P_i}{\lambda+\dfrac{\rho}{\Lambda_i}\varepsilon}\mathrm{e}^{-\frac{\rho}{\Lambda_i}x}\left[1-\mathrm{e}^{-\left(\lambda+\frac{\rho}{\Lambda_i}\varepsilon\right)t}\right], \tag{3}$$

where $C(x, \varepsilon, t)$ is the nuclide concentration (at g^{-1}), $C(x, 0)$ is the initial nuclide concentration (at g^{-1}), x is the depth (cm), ρ is the density (g cm^{-3}), λ is the decay constant 5.00×10^{-7} yr^{-1} for ^{10}Be (Chmeleff et al., 2010; Korschinek et al., 2010) and 9.83×10^{-7} yr^{-1} for ^{26}Al (Nishiizumi, 2004), P_i is the surface production rate (at g^{-1} yr^{-1}), and Λ_i is the effective attenuation length.

For surface samples (x=0) under the assumption of steady-state denudation ($t >> 1/(\lambda+\rho\varepsilon/\Lambda)$) and the contribution of muons are negligible, eq. (3) then becomes (Lal, 1991):

$$C(\varepsilon) = \frac{P_{\mathrm{spal}}}{\lambda+\dfrac{\rho}{\Lambda_{\mathrm{spal}}}\varepsilon}. \tag{4}$$

If the sediments are buried deeply and rapidly enough to prevent TCN production after burial and the burial age is not significantly older than the paired cosmogenic nuclides half-life, paired nuclides can be used to yield the burial age and pre-burial basin denudation rate, which can be described by the following equation (Granger and Muzikar, 2001; Balco and Shuster, 2009a):

$$C(\varepsilon,t_{\mathrm{b}})_m = \frac{P_m}{\lambda_m+\dfrac{\rho}{\Lambda_{\mathrm{spal}}}\varepsilon}\mathrm{e}^{-\lambda_m t_{\mathrm{b}}}, \tag{5a}$$

$$C(\varepsilon,t_{\mathrm{b}})_n = \frac{P_n}{\lambda_n+\dfrac{\rho}{\Lambda_{\mathrm{spal}}}\varepsilon}\mathrm{e}^{-\lambda_n t_{\mathrm{b}}}, \tag{5b}$$

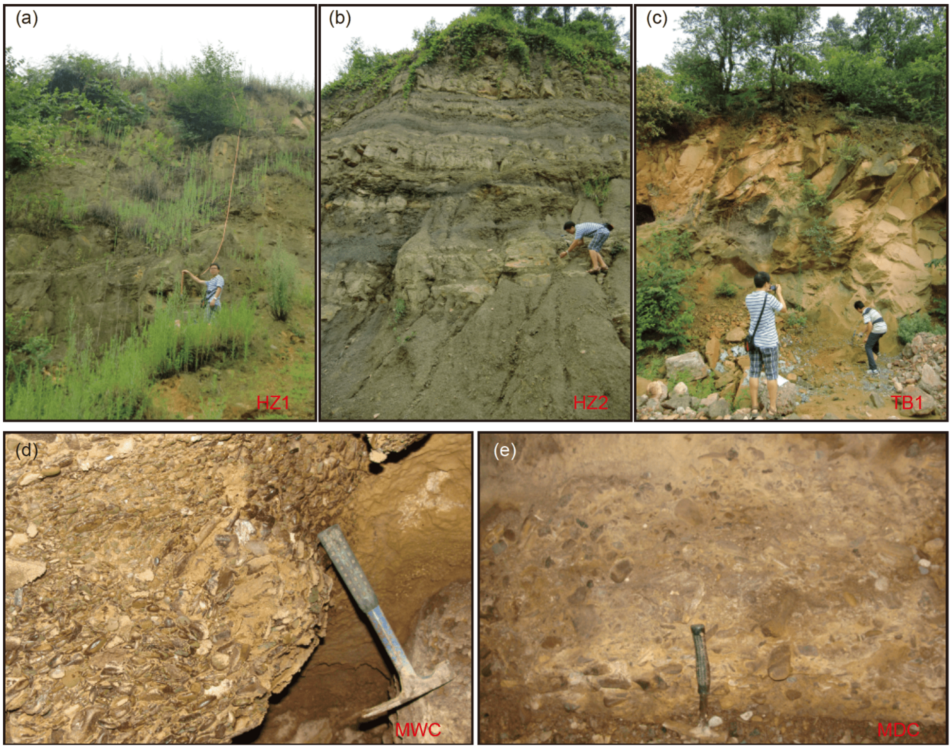

Figure 3 Field photographs of samples HZ1, HZ2, TB1, MWC, and MDC.

where m and n represent the paired nuclides, such as the ^{26}Al-^{10}Be and ^{21}Ne-^{10}Be pair, P_m and P_n are the averaged basin-wide production rate, t_b is the burial age, Λ_{spal} is the effective attenuation length for spallogenic production (here taken to be 160 g cm^{-2}), and ε is the pre-burial basin denudation rate. The basin production rates scaling factor relative to sea level and high latitude (SLHL) as a function of geographic latitude and air pressure (Lal, 1991; Stone, 2000) are listed in Table 1. We use the SLHL spallogenic production rate of 4.01 at g^{-1} yr^{-1} for ^{10}Be (Borchers et al., 2016), and the spallogenic production ratios of 6.75 for ^{26}Al/^{10}Be (Balco and Rovey, 2008) and 4.01 for ^{21}Ne/^{10}Be (Kober et al., 2011), respectively.

For the ^{26}Al-^{10}Be pair, substituting eq. (5a) into eq. (5b), we can get a transcendental equation with two free parameters (pre-burial basin denudation rate and burial age). A Monte Carlo simulation is performed to determine the denudation rate and burial age. For each measured data pair ($C_m \pm \sigma_m$ and $C_n \pm \sigma_n$), a set of 5,000 random concentrations were made for nuclides m and n with the assumption of following the normal distribution of (C_m, σ_m) and (C_n, σ_n), where C_m and C_n are the measured concentration, σ_m and σ_n are the analytical uncertainties. The concentration made in each pair was solved for denudation rate and burial age using Newton's method, and error envelopes were bounded by the confidence level of 1σ. For the ^{10}Be-^{21}Ne pair (λ_{21} = 0), substituting eq. (5a) into eq. (5b), an algebraic equation can be directly solved.

3.3 Post-burial production of cosmogenic nuclides for HZ1

For the subsurface (10 m in depth) sample of HZ1, as well as HZ2 and TB1, the post-burial productions are non-negligible. The steady-state denudation model was used to estimate the main contribution from muons, as follows:

$$C(\varepsilon) = \sum_{i=\text{spal,slow,fast}} \frac{P_i}{\lambda + \dfrac{\rho}{\Lambda_i}\varepsilon} \mathrm{e}^{-\frac{\rho}{\Lambda_i}x}, \tag{6}$$

where x is the depth of 1000 cm, and ρ is the density of 2.6 g cm^{-3}. For cosmogenic ^{10}Be, P_{spal} (9.51 at g^{-1} yr^{-1}), P_{slow} (0.1844 at g^{-1} yr^{-1}), P_{fast} (0.0728 at g^{-1} yr^{-1}) and Λ_{spal} (160 g cm^{-2}), Λ_{slow} (977 g cm^{-2}), Λ_{fast} (3642 g cm^{-2}) are the surface production rates and attenuation lengths of neutrons, slow muons, and fast muons, respectively (Balco, 2017; Yang et al., 2020). The denudation rate can be solved by eq. (6), then the post-burial production of cosmogenic ^{21}Ne can be roughly determined with the assumption of zero slow muon capture production and fast muon production rate of 0.2 at g^{-1} yr^{-1} at sea level (Fernandez-Mosquera et al., 2008; Balco et al., 2019):

$$C(\varepsilon) = \sum_{i=\text{spal,fast}} \frac{P_i}{\lambda + \dfrac{\rho}{\Lambda_i}\varepsilon} \mathrm{e}^{-\frac{\rho}{\Lambda_i}x}, \tag{7}$$

where Λ_{spal} and Λ_{fast} are equal to 160 and 4320 g cm^{-2}, respectively. The P_{spal} and P_{fast} are calculated according to the scaling factor of 2.36 (Stone, 2000).

4. Results

4.1 ^{10}Be and ^{26}Al concentrations, burial ages, and pre-burial basin denudation rates

The results of the cosmogenic nuclide ^{10}Be and ^{26}Al are listed in Tables 1 and 2. ^{10}Be and ^{26}Al concentrations in samples SXC-RB, DSC-RB, YTGC-RB, SXC, DYC, DSC, DSC-S, and YTGC are from Liu et al. (2013b) and those in HC from Liu et al. (2013a). The measured ^{10}Be concentrations vary from 8.14×10^{4} to 5.76×10^{5} at g^{-1} with the analytical uncertainties better than 4%, except for the SXC cave deposit (20.6% with a low concentration of 6.1×10^{3} at g^{-1}), the HC cave deposit (6.9% with a low concentration of 33.5×10^{3} at g^{-1}), and HZ1 bedrock (25.6% with a low concentration of 6.8×10^{3} at g^{-1}) (Table 2). The analytical uncertainties of ^{26}Al excluding SXC (42.4%), DYC (9.3%), and HC (9.2%) are better than 5%. The burial ages and pre-burial basin denudation rates according to the approaches and parameters are recalculated and described in Section 3.2. The results show that the burial ages are similar to the previous studies (Liu et al., 2013a, 2013b), but the pre-burial denudation rates are much higher because the averaged basin elevation (used to calculate basin-wide denudation rate) rather than the sampling site elevation (used to calculate local surface denudation rate) was used. For modern river sediments, MDC-RB and DSC-RB show the burial ages of $0.00^{+0.08}_{-0.00}$ and $0.00^{+0.10}_{-0.00}$ Ma, respectively, suggesting that both samples experienced a continuous exposure process. However, SXC-RB and YTGC-RB might have experienced a complex burial history with the burial ages of $0.25^{+0.10}_{-0.11}$ and $0.34^{+0.12}_{-0.11}$ Ma, respectively. For the cave deposits, all data show an obvious decay of nuclides with the ^{26}Al/^{10}Be ratios lower than 6, suggesting the samples experienced a burial history. The relatively high burial age of SXC ($1.45^{+1.13}_{-0.87}$ Ma) was represented as the results of pre-burial strong erosion events and/or large uncertainty of TCN concentration (Liu et al., 2013b). In addition, such low nuclides concentration and ^{26}Al/^{10}Be ratio can also be the result of recycled sedimentation. For the sub-surface bedrocks, only HZ1 was measured for ^{10}Be, showing that the muons contribution is non-negligible in such depths of about 10 m. A steady-state assumption is made to estimate the contribution of cosmogenic ^{21}Ne to a total excess ^{21}Ne in the next section. The pre-burial basin denudation rates excluding the SXC samples with an extremely high value of 580 mm kyr^{-1} range from ~5.8 to 68.6 mm kyr^{-1}, consistent with the carbonate surface denudation rates derived from cosmogenic ^{36}Cl (Xu et al., 2013; Yang et al., 2020) (Figure 4a).

4.2 Neon isotope ratios

Results of the three-isotopes of neon are listed in Tables 1 and 2. The measured ^{21}Ne concentrations range from 3.1×10^{6} to 14.4×10^{6} at g^{-1}. All neon isotope ratios data lie on the spallation line within the 1σ analytical uncertainty in the neon three-isotope diagram (Figure 5). However, due to the high-abundance atmospheric Ne in sediments and relatively low measurement precision of isotope ^{22}Ne, it is hard to discriminate between cosmogenic and nucleogenic components based on their Ne isotopic signatures in those samples. The ^{10}Be-^{21}Ne pair burial ages are extremely older than the ^{26}Al-^{10}Be pair burial ages, suggesting that non-cosmogenic components might take a major part in total excess Ne in all samples (Figure 4 and Table 2). The cosmogenic ^{21}Ne is computed by assuming a pre-burial ^{21}Ne/^{10}Be production ratio of 4.01±0.17 (Kober et al., 2011) and a steady-state denudation rate derived from the ^{26}Al-^{10}Be pair, then the nucleogenic ^{21}Ne is calculated by subtracting the cosmogenic ^{21}Ne from the total excess ^{21}Ne. This correlation in-

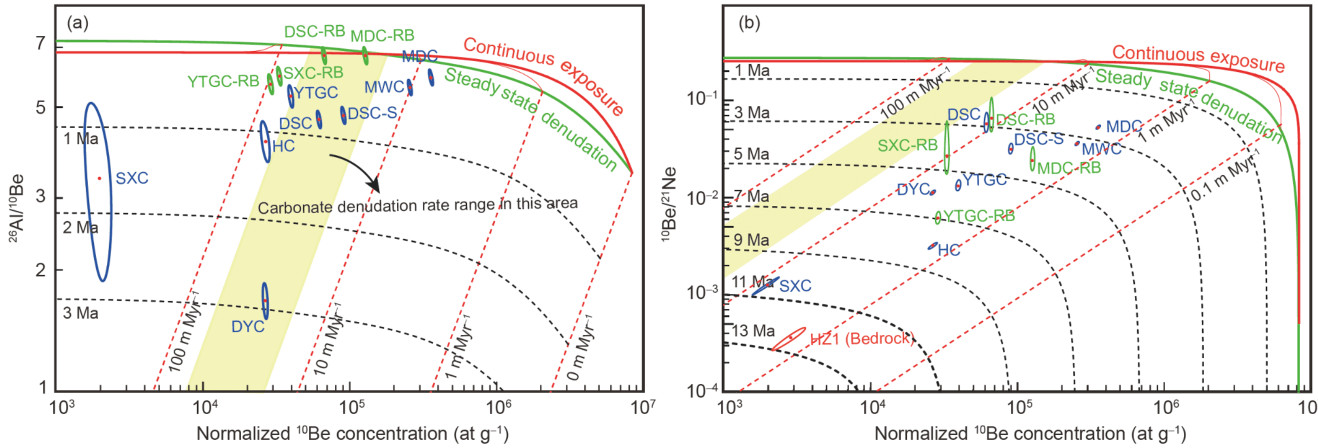

Figure 4 Normalized ^{26}Al/^{10}Be and ^{10}Be/^{21}Ne ratios plotted against ^{10}Be concentrations (scaled to SLHL according to Stone (2000)). Green and blue ellipses represent modern river sediments and cave deposits with 1σ uncertainties, respectively. Shaded yellow area shows the ^{36}Cl carbonate surface denudation rates ranging from 16 to 51 mm kyr^{-1} in the study region (Xu et al., 2013; Yang et al., 2020).

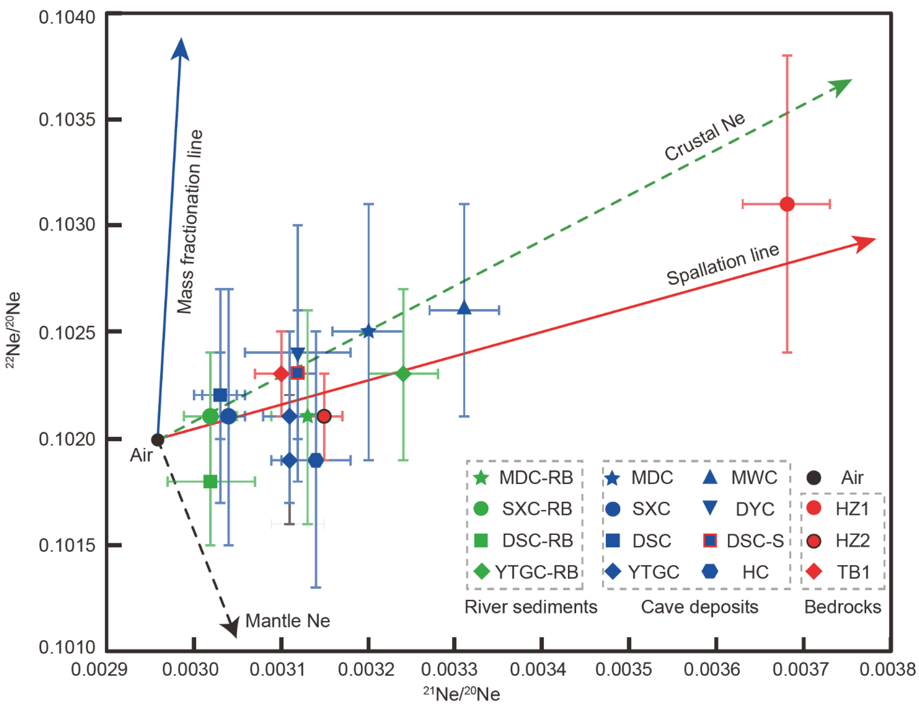

Figure 5 Neon three-isotope diagram showing the compositions and trends of various Ne components. The red solid line represents the two-component mixing line between air neon with a ^{21}Ne/^{20}Ne ratio of 0.002959 and ^{22}Ne/^{20}Ne ratio of 0.102, and purely cosmogenic neon in quartz with ^{21}Ne/^{20}Ne and ^{22}Ne/^{20}Ne ratios of 0.8±0.1 and 1.01±0.13, respectively, modified from Niedermann (2002).

dicates that the majority of excess ^{21}Ne in our samples might be nucleogenic (range from 61.5% to 98.9%) (Table 2) rather than cosmogenic, which agrees with previous studies (Middleton et al., 2012; Balco et al., 2019).

4.3 Nucleogenic ^{21}Ne results

The nucleogenic ^{21}Ne can be theoretically calculated based on the U and Th concentrations in quartz. In this study, the mean and standard deviation 0.189±0.146 and 0.580±0.501 ppm for U and Th concentrations, respectively, derived from 50 previous data (Balco et al., 2019) were used. Uncertainty of the closure age was assumed to be 20% (235±47 Ma). Thus, the calculated result shows that the nucleogenic ^{21}Ne concentration of $(14.5\pm9.5)\times10^6$ at g^{-1} account for most of the excess ^{21}Ne, consistent with the estimated results by ^{26}Al-^{10}Be pair in this study (Tables 2 and 3).

4.4 Surface denudation rate and post-burial cosmogenic ^{21}Ne of HZ1

We calculated the surface denudation rate of HZ1 according to the observed ^{10}Be concentration from the 10 m deep sample with the assumption of steady-state denudation. The surface denudation rate of 74±29 mm kyr^{-1} (Table 3) derived from the Monte Carlo simulation is roughly similar to the pre-burial basin denudation rates (Table 2) and ^{36}Cl carbonate denudation rates (Xu et al., 2013; Yang et al., 2020). The post-burial cosmogenic ^{21}Ne estimated by the eq. (7) suggests a negligible concentration of $(0.058\pm0.023)\times10^6$ at g^{-1} (cosmogenic) (Table 3) compared to the total excess ^{21}Ne of $(19.1\pm1.4)\times10^6$ at g^{-1}.

5. Discussion

5.1 The analyses of excess ^{21}Ne

The stable cosmogenic ^{21}Ne has been expected to be widely applied in surface Earth sciences as the ^{21}Ne measurements on mass spectrometers are considerably less expensive than AMS and require less quartz material. However, the complex composition of excess ^{21}Ne in quartz significantly restricts the applications. Although our neon isotope ratios data lie on the spallation line within the 1σ analytical uncertainty in the neon three-isotope diagram (Figure 5), the precision of ^{22}Ne measurements is insufficient to distinguish nucleogenic from cosmogenic ^{21}Ne enrichments in the presence of much larger amounts of atmospheric Ne (Middleton et al., 2012; Balco et al., 2019). Stepwise heating is one possible method for discriminating between cosmogenic and non-cosmogenic components. However, the nucleogenic ^{21}Ne can be released during extraction at temperatures below 600°C and above 800°C (Niedermann, 2002). Previous works such as Vermeesch et al. (2015) have summed all gases releasing from stepwise heating experiments when samples were exclusively composed of atmospheric and cosmogenic neon.

While, other works, such as Balco et al. (2019) and Balter-Kennedy et al. (2020), which have also adopted the stepwise gas extraction, cannot calculate the cosmogenic Ne contribution accurately either, due to limited constraints on releasing of nucleogenic ^{21}Ne. Alternatively, they have appealed to nucleogenic Ne correction for the total excess Ne to obtain cosmogenic Ne concentration. Considering the reasons mentioned above, we have adopted a one-step heating method in this study and attempted to correct the possible influence of nucleogenic Ne. In theory, there are two methods to estimate the nucleogenic ^{21}Ne concentrations from excess ^{21}Ne including (1) Xe and/or Ar measurement with the assumption of simultaneous Ne and Xe (Ar) closure (Fujioka et al., 2005; Middleton et al., 2012), and (2) U and Th measurement with an assumed quartz closure age (Balco et al., 2019). The latter method has been used to estimate the bedrock sandstones nucleogenic ^{21}Ne based on eq. (2). Because the geological closure temperature of (U-Th)/Ne in quartz is about 94°C (Shuster and Farley, 2005), the reheating mineralization event in relation to the formation of ~235 Ma Pb-Zn deposits in this area (Hu and Zhou, 2012) is assumed as the closure age and uncertainty was considered to be 20%. For the bedrock HZ1, the high nucleogenic ^{21}Ne concentration of (14.5±9.5)×10^6 at g^{-1} (Table 3) agrees with the inversion result (Table 2) from ^{10}Be surface denudation rate with steady-state assumption. The inherited component, henceforth called "inherited cosmogenic ^{21}Ne", may be produced during the exposure and transport process after the reheating events for cave deposits and modern river sediments. However, the inherited cosmogenic ^{21}Ne in the bedrock (HZ1, HZ2, and TB1) can be ignored due to the inventory ^{21}Ne being lost during the reheating mineralization event in this area. In order to exclude the possibility of post-burial production, the ^{10}Be concentration in HZ1 was measured to estimate the concentration of post-burial cosmogenic ^{21}Ne by eqs. (6) and (7). The negligible post-burial production of (0.058±0.023)×10^6 at g^{-1} compared to the total excess ^{21}Ne of (19.1±1.4)×10^6 at g^{-1} indicates that most of ^{21}Ne are composed by nucleogenic ^{21}Ne or inheritance produced between the reheating mineralization event and the Jurassic stratigraphic sequence age.

The decoupling relationship of burial ages and pre-burial basin denudation between the ^{26}Al-^{10}Be pair and ^{21}Ne-^{10}Be pair (Figure 4 and Table 2) indicates that the nucleogenic and/or inherited cosmogenic ^{21}Ne is non-negligible in our cave deposits and modern river sediments. The pre-burial denudation rates derived from the ^{21}Ne-^{10}Be pair are obviously lower than the surface denudation evidence from the ^{26}Al-^{10}Be pair, water chemistry data (Han and Liu, 2004; Xu and Liu, 2010), and TCN ^{36}Cl (Xu et al., 2013; Yang et al., 2020) (Figure 4), which might also be caused by the overestimated cosmogenic ^{21}Ne. A compilation of previous combined ^{10}Be and ^{21}Ne data sets (Figure 6 and Appendix Table S1 online, https://link.springer.com) shows that almost all the surface samples are plotted on the continuous exposure lines with different production rates. This is because the surface samples have high production rates and negligible decay of ^{10}Be. However, all the burial samples are plotted below the continuous exposure lines due to (1) the decay of ^{10}Be (show as the gray arrow in Figure 6b) and/or (2) non-negligible nucleogenic ^{21}Ne and/or inherited cosmogenic ^{21}Ne (show as the green arrow in Figure 6b). We also find that high concentrations of ^{21}Ne$_{ex}$ (>10^7 at g^{-1}) are rarely influenced by nucleogenic ^{21}Ne due to the relatively high concentration of cosmogenic ^{21}Ne. As mentioned above, the neglected nucleogenic and inherited ^{21}Ne from the decay of U-Th and recycling burial history, respectively, always causes the overestimation of burial ages and underestimation of basin denudation rates. Combining with previous studies (Niedermann, 2002; Ben-Israel et al., 2018; Ma and Stuart, 2018; Balco et al., 2019), we suggest that the precise calculation of the cosmogenic ^{21}Ne could be reached by (1) estimating the contribution from nucleogenic ^{21}Ne, (2) avoiding samples with complex burial histories to exclude inherited cosmogenic ^{21}Ne, and (3) combining the ^{10}Be-^{26}Al-^{21}Ne nuclides method for the Quaternary samples.

Table 3 Results of the nucleogenic ^{21}Ne and surface denudation rate in site HZ1

Parameters	Value
[U]$^{a)}$ (ppm)	0.189±0.146
[Th]$^{a)}$ (ppm)	0.580±0.146
Nucleogenic ^{21}Ne$^{b)}$ (×10^6 at g^{-1})	14.5±9.5
Surface denudation rate$^{c)}$ (mm kyr^{-1})	74±29
Post-burial produced ^{21}Ne$^{d)}$ (×10^6 at g^{-1})	0.058±0.023

a) Mean and standard deviation results are calculated from Balco et al. (2019). b) Derived from the eq. (2) with the assumption of 235±47 Ma closure age. c) Determined by the ^{10}Be concentration with the assumption of steady-state denudation. d) Calculated by the eqs. (6) and (7).

5.2 Quaternary landscape evolution in the Guizhou Plateau

Cosmogenic ^{21}Ne has been used to determine the surface denudation rates of fluvial sediments with the assumption of a steady-state denudation model. However, the nucleogenic and inherited cosmogenic ^{21}Ne from fluvial sediments are non-negligible because it is a stable isotope and does not decay. The overestimated cosmogenic ^{21}Ne may cause underestimated surface denudation rates or overestimated exposure ages (Hetzel et al., 2002; Graf et al., 2007; Codilean et al., 2008; Strasky et al., 2009; Ma et al., 2016). Depth profile is a good way to distinguish the present cosmogenic ^{21}Ne from inheritance and nucleogenic ^{21}Ne (Phillips et al., 1998; Ma et al., 2016). However, it is invalid for the burial samples due to the lack of post-burial production. In our study region,

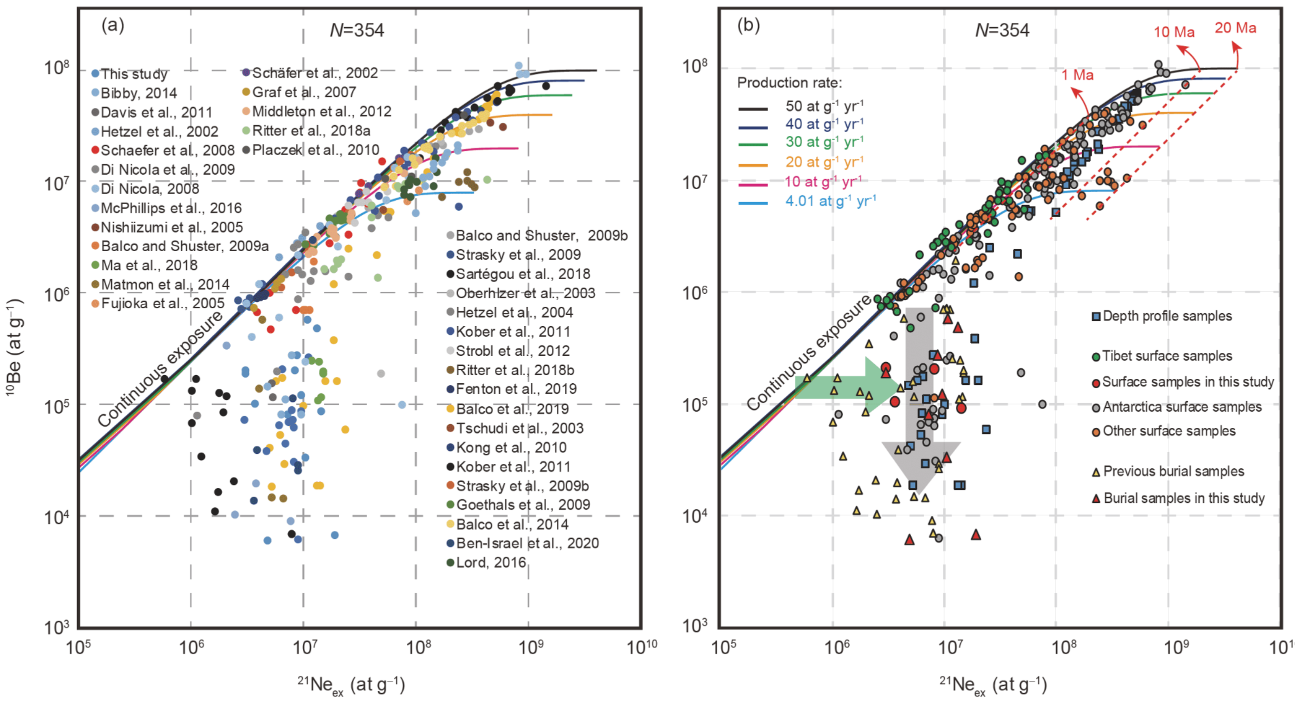

Figure 6 Integrated previous ^{10}Be-^{21}Ne data are plotted according to (a) different previous works and (b) sample types. Colored curves are traced by irradiating a rock of zero denudation (continuous exposure lines). Dashed red lines indicate the exposure duration. Gray and green arrows present the decay of ^{10}Be and the existence of nucleogenic and/or inherited ^{21}Ne, respectively. Details of references and data are presented in Appendix Table S1 online.

an approach combining the ^{10}Be-^{26}Al-^{21}Ne nuclides is carried out to determine the Quaternary landscape evolution history. The pre-burial basin denudation rates, excluding the SXC samples with an extremely high value of 580 mm kyr^{-1} and the MWC and MDC with the lower values, range from ~18.3 to 68.6 mm kyr^{-1} (mean 39±18 mm kyr^{-1}), which is consistent with the carbonate surface denudation rates derived from cosmogenic ^{36}Cl (16–51 mm kyr^{-1}) (Xu et al., 2013; Yang et al., 2020) and water chemistry data (30–42 mm kyr^{-1}) (Han and Liu, 2004; Xu and Liu, 2010) (Figure 4). The HZ1 modern surface denudation rate of 74 mm kyr^{-1} (Table 3) derived from eq. (6) with an assumption of steady-state denudation also shows a similar result. The Liuchonghe and Sanchahe watersheds fluvial incision rates of $53.2^{+4.1}_{-3.9}$ and $42.6^{+13.8}_{-9.1}$ mm kyr^{-1} (Figure 7), respectively, are slightly higher than the surface denudation rate, which might be the result of the regional tectonic uplift. However, the Luoanjiang watershed presents a high fluvial incision rate (259^{+59}_{-63} mm kyr^{-1}) (Figure 7) and low pre-burial basin denudation rates (Table 2), suggesting that the fluvial retreat in this local area might have started relatively later than elsewhere, but the fluvial dynamics is stronger since the late Quaternary (Table 2), and/or a strong tectonic uplift controlled by Zunyi fault in Luoanjiang area (Figure 1b). Our fluvial incision rates, as well as surface denudation rates derived from ^{36}Cl, show that the incision/ denudation rates are higher in the western and central Guizhou highlands and lower in the eastern lowlands (Figure 1b). The results show that the regional variation in incision/denudation rates is likely controlled by stronger tectonic uplift and fluvial retreat in the western and central Guizhou Plateau. In summary, the consistency of the different timescales pre-burial basin denudation rate, ^{36}Cl surface denudation rate, water chemistry data, and modern basin denudation rate suggests that the landscape-scale surface denudation has been stabilized since the Quaternary. The slightly higher incision rates excluding the most eastern sample HC than the surface local denudation rate show that the river dynamics may not have reached steady-state due to the regional tectonic uplift.

6. Conclusions

Based on the ^{10}Be-^{26}Al-^{21}Ne nuclides measurements from cave deposits, modern river sediments and bedrock sandstones from the Guizhou Plateau, we conclude that: (1) The contribution from nucleogenic and/or inherited cosmogenic ^{21}Ne in sediments quartz is non-negligible, (2) the consistency of the different timescale surface denudation rates suggest that the landscape-scale surface denudation rate is relatively stable during the Quaternary in the Guizhou Plateau, and (3) the tectonic uplift plays an important role in modulating the landscape evolution in the Guizhou Plateau.

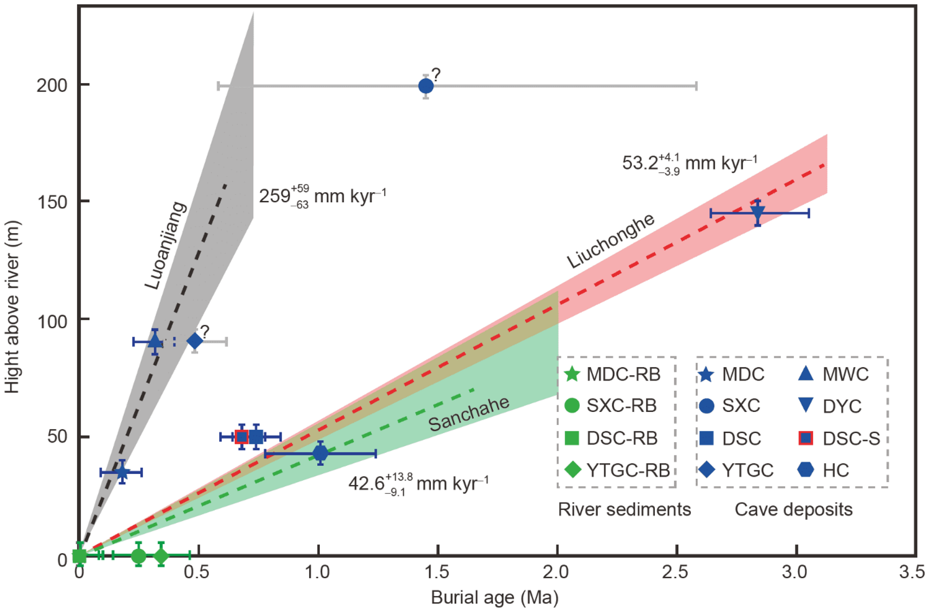

Figure 7 Fluvial incision rates in the Guizhou Plateau. Red, black, and green dashed lines excluding two outliers (SXC and YTGC) show the best-fitted river incision rates of the Liuchonghe, Luoanjiang, and Sanchahe rivers, respectively. Shaded areas represent the uncertainties. The incision rates are calculated by Monte Carlo methods with 1σ confidence level.

Acknowledgements *Constructive comments by responsible editor and two anonymous reviewers significantly improved the paper. We are grateful to Dr L. Di Nicola for help in the Ne isotope measurement. This work was supported by the National Natural Science Foundation of China (Grant No. 41930642).*

References

Balco G. 2017. Production rate calculations for cosmic-ray-muon-produced ^{10}Be and ^{26}Al benchmarked against geological calibration data. Quat-Geochronol, 39: 150–173

Balco G, Blard P H, Shuster D L, Stone J O H, Zimmermann L. 2019. Cosmogenic and nucleogenic ^{21}Ne in quartz in a 28-meter sandstone core from the McMurdo Dry Valleys, Antarctica. Quat Geochronol, 52: 63–76

Balco G, Rovey C W. 2008. An isochron method for cosmogenic-nuclide dating of buried soils and sediments. Am J Sci, 308: 1083–1114

Balco G, Shuster D L. 2009a. ^{26}Al-^{10}Be-^{21}Ne burial dating. Earth Planet Sci Lett, 286: 570–575

Balco G, Shuster D L. 2009b. Production rate of cosmogenic ^{21}Ne in quartz estimated from ^{10}Be, ^{26}Al, and ^{21}Ne concentrations in slowly eroding Antarctic bedrock surfaces. Earth Planet Sci Lett, 281: 48–58

Balter-Kennedy A, Bromley G, Balco G, Thomas H, Jackson M S. 2020. A 14.5-million-year record of East Antarctic ice sheet fluctuations from the central transantarctic mountains, constrained with cosmogenic ^{3}He, ^{10}Be, ^{21}Ne, and ^{26}Al. Cryosphere, 14: 2647–2672

Ben-Israel M, Matmon A, Haviv I, Niedermann S. 2018. Applying stable cosmogenic ^{21}Ne to understand surface processes in deep geological time (10^7–10^8 yr). Earth Planet Sci Lett, 498: 266–274

Ben-Israel M, Matmon A, Hidy A J, Avni Y, Balco G. 2020. Early-to-mid Miocene erosion rates inferred from pre-Dead Sea rift Hazeva River fluvial chert pebbles using cosmogenic ^{21}Ne. Earth Surf Dynam, 8: 289–301

Borchers B, Marrero S, Balco G, Caffee M, Goehring B, Lifton N, Nishiizumi K, Phillips F, Schaefer J, Stone J. 2016. Geological calibration of spallation production rates in the CRONUS-Earth project. Quat Geochronol, 31: 188–198

Chmeleff J, von Blanckenburg F, Kossert K, Jakob D. 2010. Determination of the ^{10}Be half-life by multicollector ICP-MS and liquid scintillation counting. Nucl Instrum Meth Phys Res Sect B-Beam Interact Mater Atoms, 268: 192–199

Clark M K, House M A, Royden L H, Whipple K X, Burchfiel B C, Zhang X, Tang W. 2005. Late Cenozoic uplift of southeastern Tibet. Geology, 33: 525–528

Clark M K, Schoenbohm L M, Royden L H, Whipple K X, Burchfiel B C, Zhang X, Tang W, Wang E, Chen L. 2004. Surface uplift, tectonics, and erosion of eastern Tibet from large-scale drainage patterns. Tectonics, 23: TC1006

Codilean A T, Bishop P, Stuart F M, Hoey T B, Fabel D, Freeman S P H T. 2008. Single-grain cosmogenic ^{21}Ne concentrations in fluvial sediments reveal spatially variable erosion rates. Geology, 36: 159–162

Cox S E, Farley K A, Cherniak D J. 2015. Direct measurement of neon production rates by (α, n) reactions in minerals. Geochim Cosmochim Acta, 148: 130–144

Davis M, Matmon A, Fink D, Ron H, Niedermann S. 2011. Dating Pliocene lacustrine sediments in the central Jordan Valley, Israel—Implications for cosmogenic burial dating. Earth Planet Sci Lett, 305: 317–327

Dunai T J. 2010. Cosmogenic Nuclides: Principles, Concepts and Applications in the Earth Surface Sciences. Cambridge: Cambridge University Press

Eberhardt P, Eugster O, Marti K. 1965. Notizen: A redetermination of the isotopic composition of atmospheric Neon. Zeitschrift für Naturforschung A, 20: 623–624

Fernandez-Mosquera D, Marti H, Hahm D, Vidal-Romani J, Braucher R, Bourlès D. 2008. Muon produced neon in quartz at large depths: BeNe project progress report. Geochim Cosmochim Acta, 72: A265

Fujioka T, Chappell J, Honda M, Yatsevich I, Fifield K, Fabel D. 2005. Global cooling initiated stony deserts in central Australia 2–4 Ma, dated by cosmogenic ^{21}Ne-^{10}Be. Geology, 33: 993–996

Gosse J C, Phillips F M. 2001. Terrestrial *in situ* cosmogenic nuclides: Theory and application. Quat Sci Rev, 20: 1475–1560

Graf A A, Strasky S, Ivy-Ochs S, Akçar N, Kubik P W, Burkhard M, Schlüchter C. 2007. First results of cosmogenic dated pre-Last Glaciation erratics from the Montoz area, Jura Mountains, Switzerland. Quat Int, 164-165: 43–52

Granger D E, Muzikar P F. 2001. Dating sediment burial with *in situ*-

produced cosmogenic nuclides: Theory, techniques, and limitations. Earth Planet Sci Lett, 188: 269–281

Han G, Liu C Q. 2004. Water geochemistry controlled by carbonate dissolution: A study of the river waters draining karst-dominated terrain, Guizhou Province, China. Chem Geol, 204: 1–21

Heber V S, Wieler R, Baur H, Olinger C, Friedmann T A, Burnett D S. 2009. Noble gas composition of the solar wind as collected by the Genesis mission. Geochim Cosmochim Acta, 73: 7414–7432

Hetzel R, Niedermann S, Ivy-Ochs S, Kubik P W, Tao M, Gao B. 2002. ^{21}Ne versus ^{10}Be and ^{26}Al exposure ages of fluvial terraces: The influence of crustal Ne in quartz. Earth Planet Sci Lett, 201: 575–591

Hu R Z, Zhou M F. 2012. Multiple Mesozoic mineralization events in South China—An introduction to the thematic issue. Miner Depos, 47: 579–588

Kober F, Alfimov V, Ivy-Ochs S, Kubik P W, Wieler R. 2011. The cosmogenic ^{21}Ne production rate in quartz evaluated on a large set of existing ^{21}Ne-^{10}Be data. Earth Planet Sci Lett, 302: 163–171

Kohl C P, Nishiizumi K. 1992. Chemical isolation of quartz for measurement of *in-situ*-produced cosmogenic nuclides. Geochim Cosmochim Acta, 56: 3583–3587

Korschinek G, Bergmaier A, Faestermann T, Gerstmann U C, Knie K, Rugel G, Wallner A, Dillmann I, Dollinger G, von Gostomski C L, Kossert K, Maiti M, Poutivtsev M, Remmert A. 2010. A new value for the half-life of ^{10}Be by Heavy-Ion Elastic Recoil Detection and liquid scintillation counting. Nucl Instrum Meth Phys Res Sect B-Beam Interact Mater Atoms, 268: 187–191

Lal D. 1991. Cosmic ray labeling of erosion surfaces: *In situ* nuclide production rates and erosion models. Earth Planet Sci Lett, 104: 424–439

Liu Y, Wang S J, Liu X M, Xu S, Fabel D, Luo W J. 2013a. Cosmogenic nuclides ^{26}Al and ^{10}Be burial age of Black Cave sediments, Libo of Guizhou, China. Quat Sci, 33: 437–444

Liu Y, Wang S, Xu S, Liu X, Fabel D, Zhang X, Luo W, Cheng A. 2013b. New evidence for the incision history of the Liuchong River, Southwest China, from cosmogenic ^{26}Al/^{10}Be burial ages in cave sediments. J Asian Earth Sci, 73: 274–283

Liu-Zeng J, Tapponnier P, Gaudemer Y, Ding L. 2008. Quantifying landscape differences across the Tibetan Plateau: Implications for topographic relief evolution. J Geophys Res, 113: F04018

Ma Y, Stuart F M. 2018. The use of *in-situ* cosmogenic ^{21}Ne in studies on long-term landscape development. Acta Geochim, 37: 310–322

Ma Y, Wang W, Zheng D, Zhang H, Pang J, Wu Y, Stuart F M, Xu S. 2018. Mid-Miocene cosmogenic upper limit for ^{10}Be/^{21}Ne burial age. Quat Geochronol, 48: 72–79

Ma Y, Wu Y, Li D, Zheng D, Zheng W, Zhang H, Pang J, Wang Y. 2016. Erosion rate in the Shapotou area, northwestern China, constrained by *in situ*-produced cosmogenic ^{21}Ne in long-exposed erosional surfaces. Quat Geochronol, 31: 3–11

Matmon A, Fink D, Davis M, Niedermann S, Rood D, Frumkin A. 2014. Unraveling rift margin evolution and escarpment development ages along the Dead Sea fault using cosmogenic burial ages. Quat Res, 82: 281–295

McPhillips D, Hoke G D, Liu-Zeng J, Bierman P R, Rood D H, Niedermann S. 2016. Dating the incision of the Yangtze River gorge at the First Bend using three-nuclide burial ages. Geophys Res Lett, 43: 101–110

Middleton J L, Ackert Jr. R P, Mukhopadhyay S. 2012. Pothole and channel system formation in the McMurdo Dry Valleys of Antarctica: New insights from cosmogenic nuclides. Earth Planet Sci Lett, 355-356: 341–350

Niedermann S. 2002. Cosmic-ray-produced noble gases in terrestrial rocks: Dating tools for surface processes. Rev Mineral Geochem, 47: 731–784

Nishiizumi K. 2004. Preparation of ^{26}Al AMS standards. Nucl Instrum Meth Phys Res Sect B-Beam Interact Mater Atoms, 223-224: 388–392

Phillips W M, McDonald E V, Reneau S L, Poths J. 1998. Dating soils and alluvium with cosmogenic ^{21}Ne depth profiles: Case studies from the Pajarito Plateau, New Mexico, USA. Earth Planet Sci Lett, 160: 209–223

Sartégou A, Bourlès D L, Blard P H, Braucher R, Tibari B, Zimmermann L, Leanni L, Aumaître G, Keddadouche K. 2018. Deciphering landscape evolution with karstic networks: A Pyrenean case study. Quat Geochronol, 43: 12–29

Schäfer J M, Tschudi S, Zhao Z, Wu X, Ivy-Ochs S, Wieler R, Baur H, Kubik P W, Schlüchter C. 2002. The limited influence of glaciations in Tibet on global climate over the past 170,000 yr. Earth Planet Sci Lett, 194: 287–297

Shuster D L, Farley K A. 2005. Diffusion kinetics of proton-induced ^{21}Ne, ^{3}He, and ^{4}He in quartz. Geochim Cosmochim Acta, 69: 2349–2359

Smart P L, Waltham A C, Yang M, Zhang Y. 1985. Karst Geomorphology of Western Guizhou, China. Cave Sci, 13: 89–104

Stone J O. 2000. Air pressure and cosmogenic isotope production. J Geophys Res-Solid Earth, 105: 23753–23759

Strasky S, Graf A A, Zhao Z, Kubik P W, Baur H, Schlüchter C, Wieler R. 2009. Late Glacial ice advances in southeast Tibet. J Asian Earth Sci, 34: 458–465

Vermeesch P, Balco G, Blard P H, Dunai T J, Kober F, Niedermann S, Shuster D L, Strasky S, Stuart F M, Wieler R, Zimmermann L. 2015. Interlaboratory comparison of cosmogenic ^{21}Ne in quartz. Quat Geochronol, 26: 20–28

Xu S, Liu C Q, Freeman S, Lang Y C, Schnabel C, Tu C L, Wilcken K, Zhao Z Q. 2013. *In-situ* cosmogenic ^{36}Cl denudation rates of carbonates in Guizhou karst area. Chin Sci Bull, 58: 2473–2479

Xu Z, Liu C Q. 2010. Water geochemistry of the Xijiang basin rivers, South China: Chemical weathering and CO_2 consumption. Appl Geochem, 25: 1603–1614

Yang Y, Lang Y C, Xu S, Liu C Q, Cui L F, Freeman S P H T, Wilcken K M. 2020. Combined unsteady denudation and climatic gradient factors constrain carbonate landscape evolution: New insights from *in situ* cosmogenic ^{36}Cl. Quat Geochronol, 58: 101075

Yang Y, Liu C Q, Van der Woerd J, Xu S, Cui L F, Zhao Z Q, Wang Q L, Jia G D, Chabaux F. 2019. New constraints on the late Quaternary landscape evolution of the eastern Tibetan Plateau from ^{10}Be and ^{26}Al *in-situ* cosmogenic nuclides. Quat Sci Rev, 220: 244–262

(Responsible editor: Jiafu ZHANG)